Supplement of: A coupled CH_4, CO and CO_2 simulation for improved chemical source modelling

Beata Bukosa, Jenny A. Fisher, Nicholas M. Deutscher and Dylan B. A Jones
Correspondence: Beata Bukosa (beata.bukosa@niwa.co.nz)

S1 Modifications to the public GEOS-Chem v12.1.1

There are two modifications that we implemented in our simulations (both coupled and uncoupled) that are not available in the public version of the uncoupled methane (CH_4) and carbon dioxide (CO_2) simulations. Firstly, for CH_4 we made a minor correction to the treatment of CH_4 loss. In the uncoupled CH_4 simulation, the diurnal variability of the hydroxyl radical (OH) field was neglected, which would overestimate CH_4 loss at night and underestimate it during the day, with biases of up to 100% in some regions. In other offline GEOS-Chem simulations including carbon monoxide (CO), OH concentration is scaled to the cosine of the solar zenith angle to approximate diurnal variability. We updated the CH_4 code to also apply the diurnal scaling to the OH field used for CH_4 oxidation in the troposphere. Using a 1-year test simulation for 2005, we found that this change has a negligible impact on global annual tropospheric CH_4 loss. Note, the calculation of the CH_4 loss in the stratosphere is unchanged between the coupled and uncoupled simulations. Secondly, for CO_2 we made a minor modification by updating the simulation to use The Quick Fire Emissions Dataset (QFEDv2, Darmenov and da Silva (2015)) emissions that were not available in the public version of the uncoupled v12.1.1 CO_2 simulation. We implemented this following the method used in the uncoupled CH_4 simulation to use a consistent biomass burning emission inventory across all three species. For all three gases, we use daily QFEDv2 emissions with additional diurnal scale factors. For CO, we use vertical partitioning of the emissions where 35% of the biomass burning emissions are emitted above the Planetary Boundary Layer (default setup in the uncoupled v12.1.1 CO simulation). For CO_2 and CH_4, the emissions are emitted at the surface only and transported to higher altitudes via mixing, following the v12.1.1 setup.

S2 Coupled and *coupled-origOH* differences

To understand the origin of the differences in the CO_{CH_4} (CO mole fraction from CO production from CH_4) seasonal cycles we add an additional chemical term to the analysis, $L(CO_{CH_4})$ that represents the loss of CO_{CH_4} via OH, which is a sub-component of the total $L(CO)$ (CO loss). The difference between the production ($P(CO_{CH_4})$) and loss ($L(CO_{CH_4})$) together with transport leads to the modelled CO_{CH_4} mole fractions. Figure S1 shows the global surface and 500 hPa altitude $P(CO_{CH_4})$, $L(CO_{CH_4})$ and their difference from the coupled and *coupled-origOH* simulation. Both at the surface and in the mid troposphere, the *coupled-origOH* simulation results show significantly lower production in May–September, a period

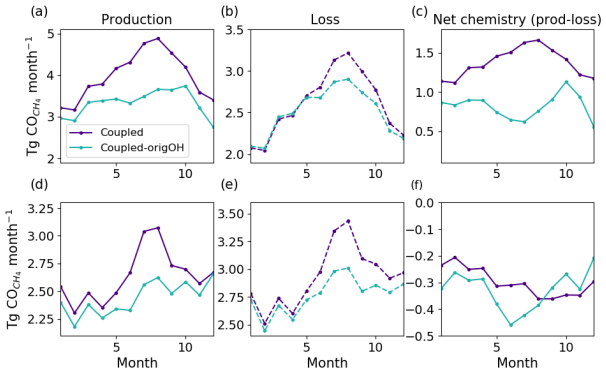


Figure S1. Global production of CO from CH_4 (a, d), its loss via OH (b, e) and their difference (c, f) in the coupled (indigo) and *coupled-origOH* (turquoise) simulations at the surface (a–c) and 500 hPa altitude (d–f) for year 2006.

when we observe the maximum production in the coupled simulation, leading to an opposite seasonal cycle. The v5-07-08 OH field used in the *coupled-origOH* simulation results in weaker $L(CH_{4Trop})$ during Northern Hemisphere (NH) summer, which leads to weaker $P(CO_{CH_4})$ and significant differences in the net chemistry (production-loss) and resulting mole fractions. We find that this difference is the most pronounced at the surface while at higher altitudes it slowly diminishes.

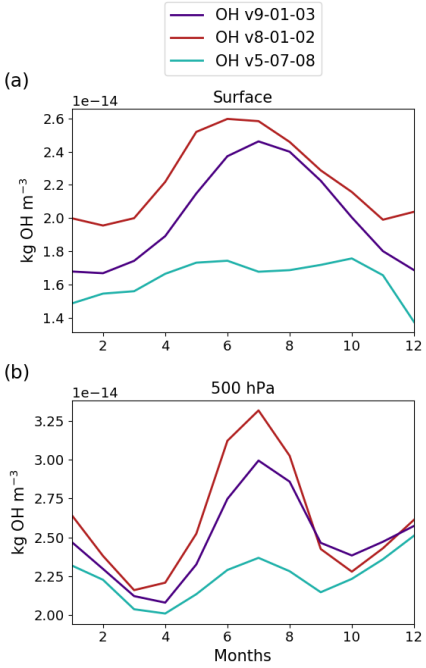


Figure S2. Globally averaged OH fields at the surface (a) and at 500 hPa (b) from the v9-01-03 (indigo, used by uncoupled CO and coupled simulation), v8-02-01 (red, uncoupled CO_2) and v5-07-08 (turquoise, uncoupled CH_4 and *coupled-origOH*) full chemistry simulations.

Table S1. GEOS-Chem emission inventories used for both the uncoupled and coupled carbon gas simulations.

	CO_2	CH_4	CO
Fields used by both uncoupled and coupled simulations			
Anthropogenic[a]	ODIAC[b]	EDGARv4.3.2[c]	EDGARv4.2
Europe	-	-	EMEP[d]
Mexico	-	CanMex[e]	BRAVO[f]
Canada	-	CanMex[e]	CAC[g]
USA	-	GEPA[h]	NEI[i]
Asia	-	-	MIX v1.1[j]
Biomass Burning	QFEDv2[k]	QFEDv2	QFEDv2
Biofuel Burning	Yevich and Logan[l]	-	Yevich and Logan
Ocean exchange	Takahashi et al.[m]	-	-
Balanced Biosphere	SIB3[n]	-	-
Net Terrestrial Exchange	TransCom[o]	-	-
Shipping	ICOADS[p]	-	ICOADS
Aviation	AEIC[q]	-	AEIC
Soil and Termites	-	Fung et al.[r]	-
Wetland	-	JPL WetCHARTs v1.0[s]	-
Seeps	-	Maasakkers et al. in prep.	-
Rice	-	EDGARv4.3.2	-
Cl sink	-	Maasakkers et al. (2019)	-

[a] The anthropogenic emissions in the CO simulation had regional overwrites for the countries specified in the table.
[b] Open-source Data Inventory of Anthropogenic CO_2 (Oda and Maksyutov, 2011) [c] European Commission. Emission Database for Global Atmospheric Research (http://edgar.jrc.ec.europa.eu/) [d] European Monitoring and Evaluation Programme (Vestreng et al., 2007) [e] Sheng et al. (2017) [f] The Big Bend Regional Aerosol and Visibility Observational Study (Kuhns et al., 2005) [g] Criteria Air Contaminants Van Donkelaar et al. (2012) [f] National Emissions Inventory (http://www.epa.gov/ttnchie1/net/2005inventory.html) [i] Maasakkers et al. (2016) [j] Li et al. (2017) [k] The Quick Fire Emissions Dataset (Darmenov and da Silva, 2015) [l] Yevich and Logan (2003) [m] Takahashi et al. (2009) [n] The Simple Biosphere (Messerschmidt et al., 2013) [o] Baker et al. (2006) [p] International Comprehensive Ocean–Atmosphere Data Set (Lee et al., 2011) [q] Aviation Emissions Inventory Code (Stettler et al., 2011) [r] Fung et al. (1991) [s] Bloom et al. (2017)

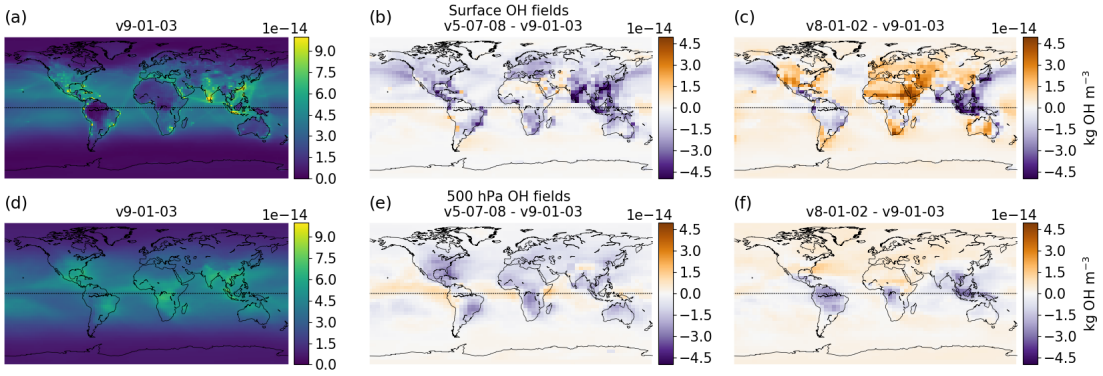


Figure S3. Surface (a–c) and 500 hPa (d–f) yearly averaged global spatial distribution of the OH fields based on the v9-01-03 (a, d) full chemistry simulation and the difference between v5-07-08 - v9-01-03 (b, e) and v8-02-01 - v9-01-03 (c, f).

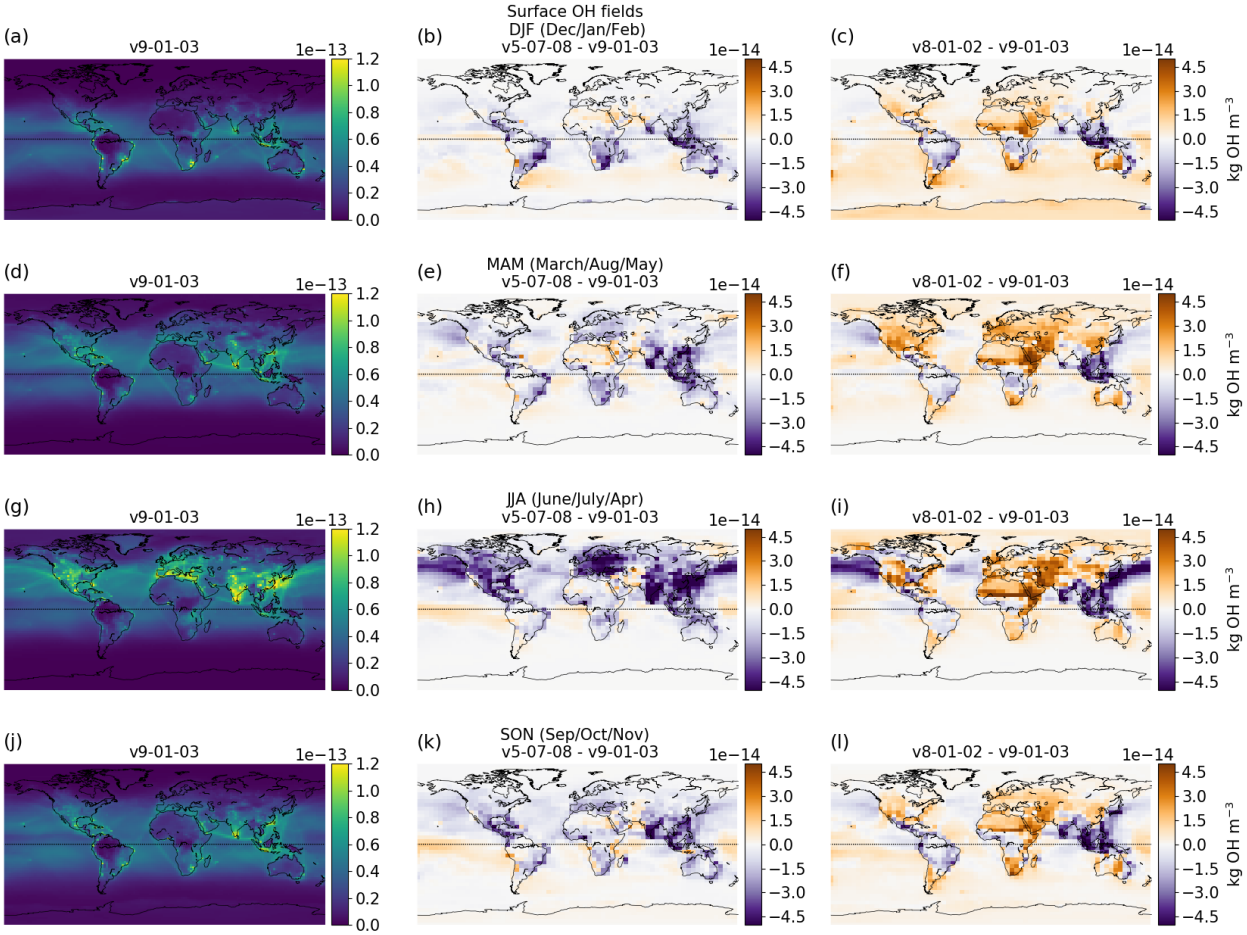


Figure S4. Surface yearly averaged global spatial distribution of the OH fields based on the v9-01-03 (a, d, g, j) full chemistry simulation and the difference between v5-07-08 - v9-01-03 (b, e, h, k) and v8-02-01 - v9-01-03 (c, f, i, l) for each season: December–January–February (DJF, a–c), March–April–May (MAM, d–f), June–July–August (JJA, g–i), September–October–November (SON, j–l).

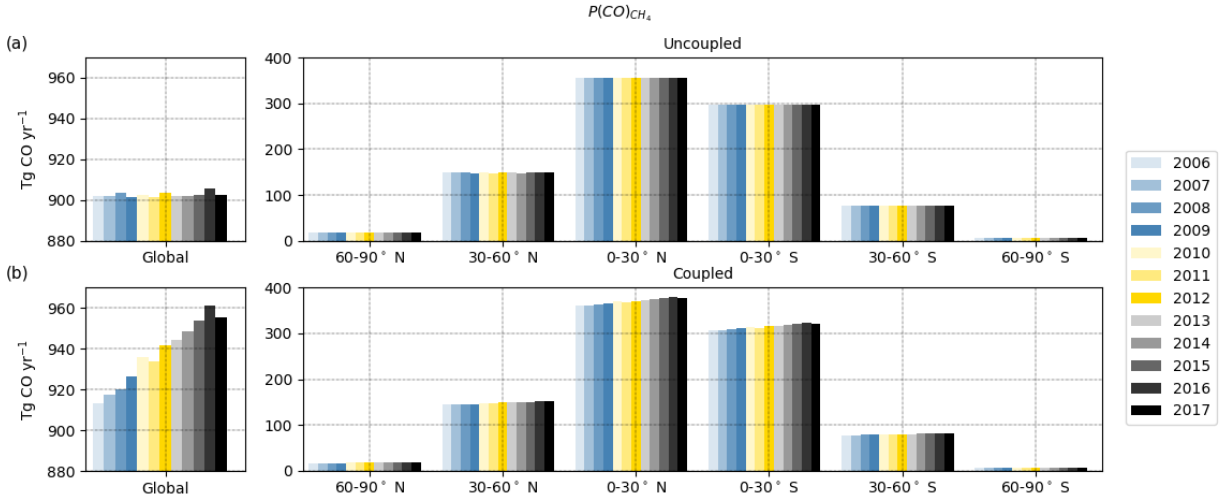


Figure S5. Annual budgets of the global and regional CO production from CH_4 from the uncoupled (a) and coupled (b) simulation.

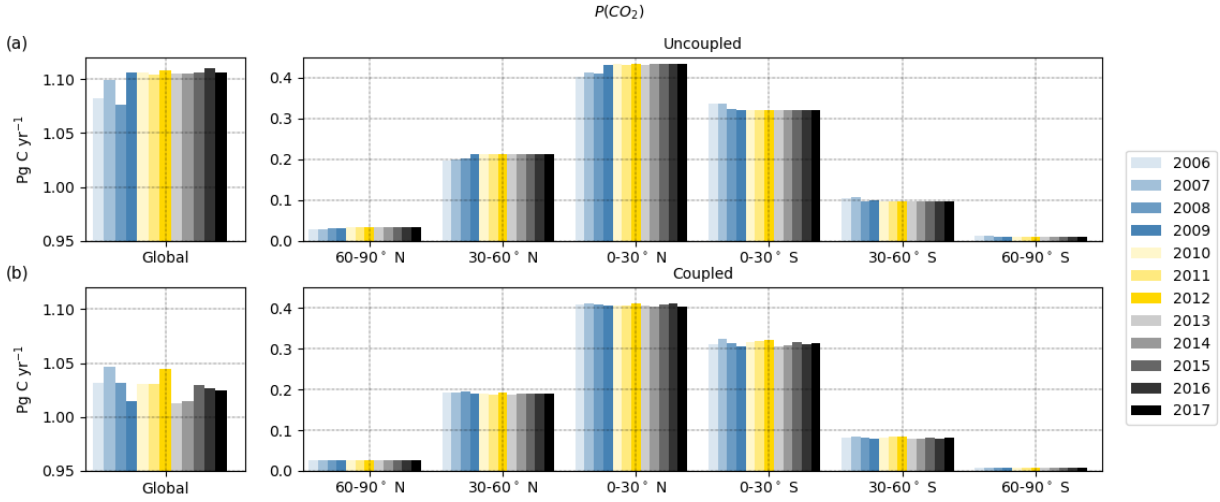


Figure S6. Annual budgets of the global and regional CO_2 production from the uncoupled (a) and coupled (b) simulations.

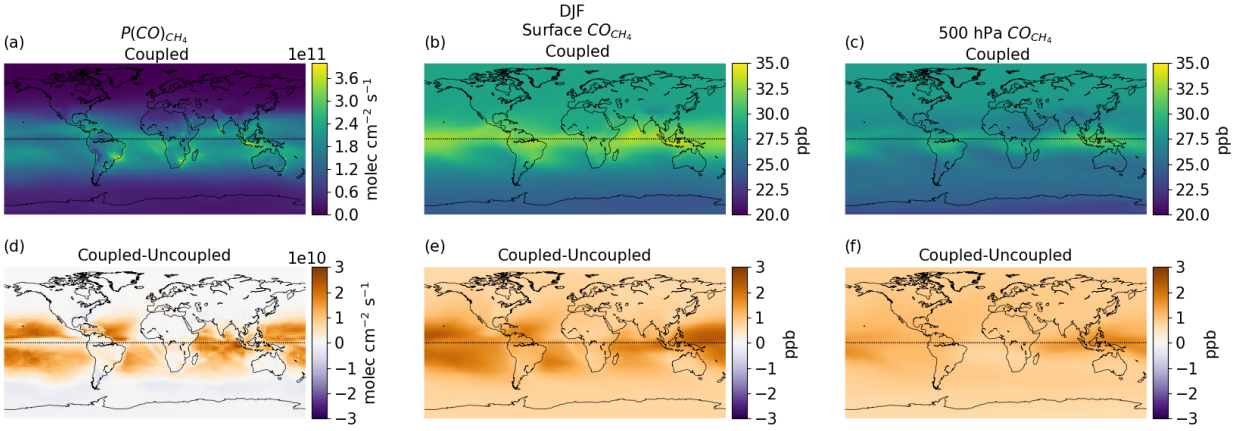


Figure S7. Average December–January–February (DJF) 2006–2017 total column CO chemical production from CH_4 (a), corresponding mole fractions (i.e., CO_{CH_4}) at the surface (b) and at 500 hPa (c) from the coupled simulation along with the difference in each field between the coupled and uncoupled simulation (d–f).

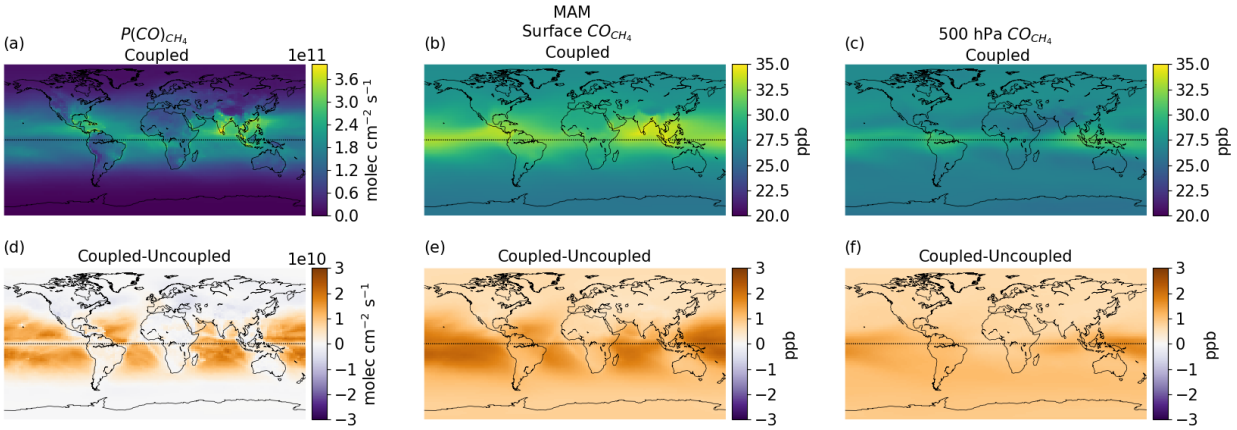


Figure S8. Average March–April–May (MAM) 2006–2017 total column CO chemical production from CH_4 (a), corresponding mole fractions (i.e., CO_{CH_4}) at the surface (b) and at 500 hPa (c) from the coupled simulation along with the difference in each field between the coupled and uncoupled simulation (d–f).

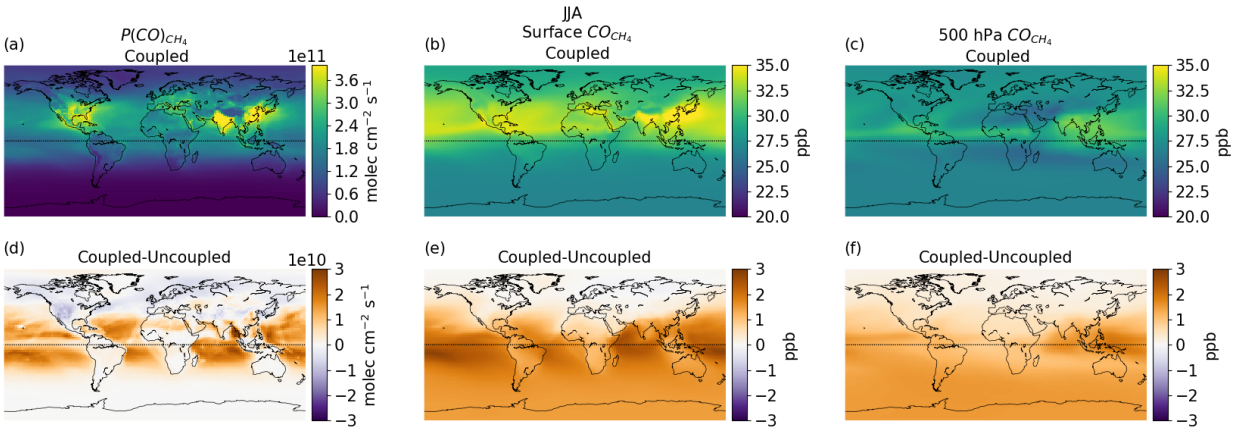


Figure S9. Average June–July–August (JJA) 2006–2017 total column CO chemical production from CH_4 (a), corresponding mole fractions (i.e., CO_{CH_4}) at the surface (b) and at 500 hPa (c) from the coupled simulation along with the difference in each field between the coupled and uncoupled simulation (d–f).

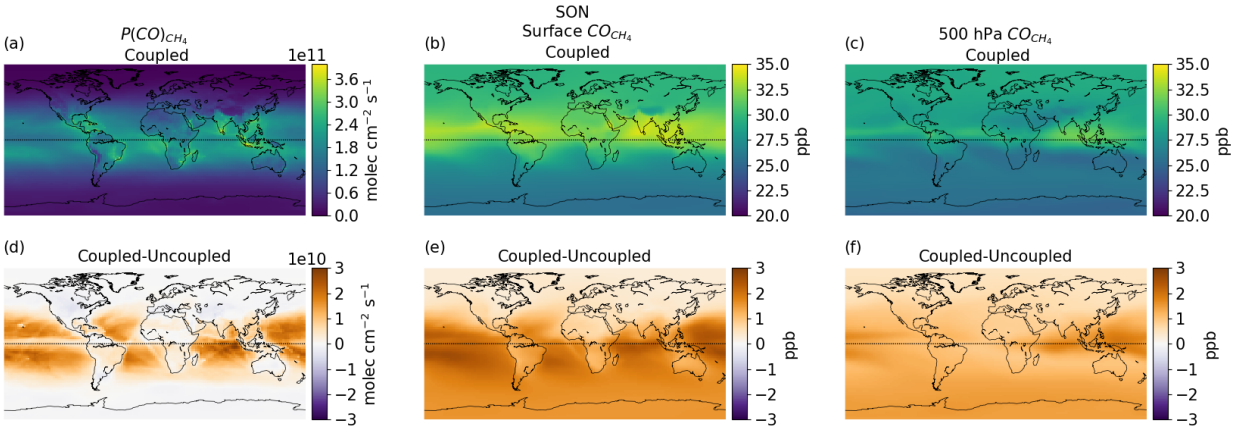


Figure S10. Average September–October–November (SON) 2006–2017 total column CO chemical production from CH_4 (a), corresponding mole fractions (i.e., CO_{CH_4}) at the surface (b) and at 500 hPa (c) from the coupled simulation along with the difference in each field between the coupled and uncoupled simulation (d–f).

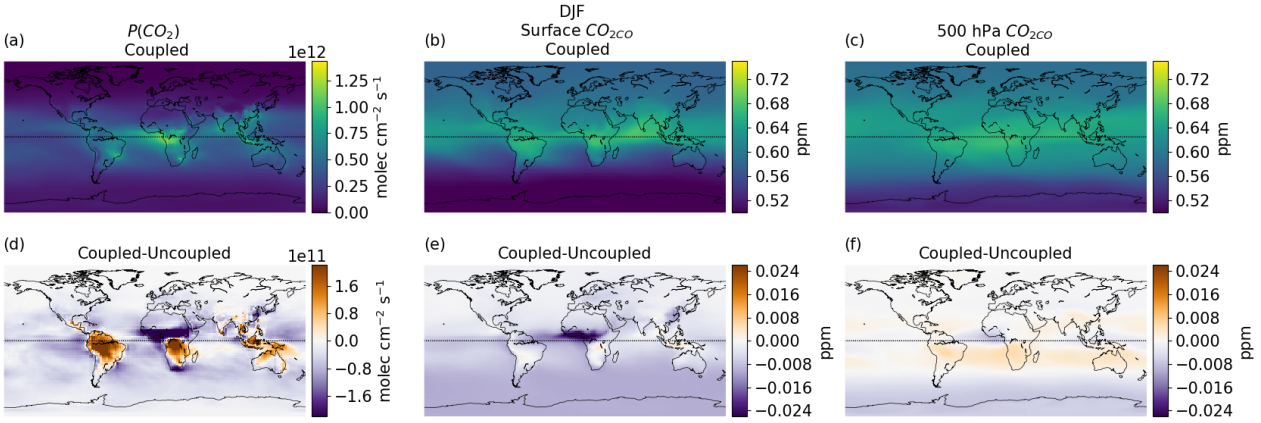


Figure S11. Average December–January–February (DJF) 2006–2017 total column CO_2 chemical production from CO (a) and corresponding mole fractions (i.e., CO_{2CO}) at the surface (b) and at 500 hPa (c) from the coupled simulation along with the difference in each field between the coupled and uncoupled simulation (d–f).

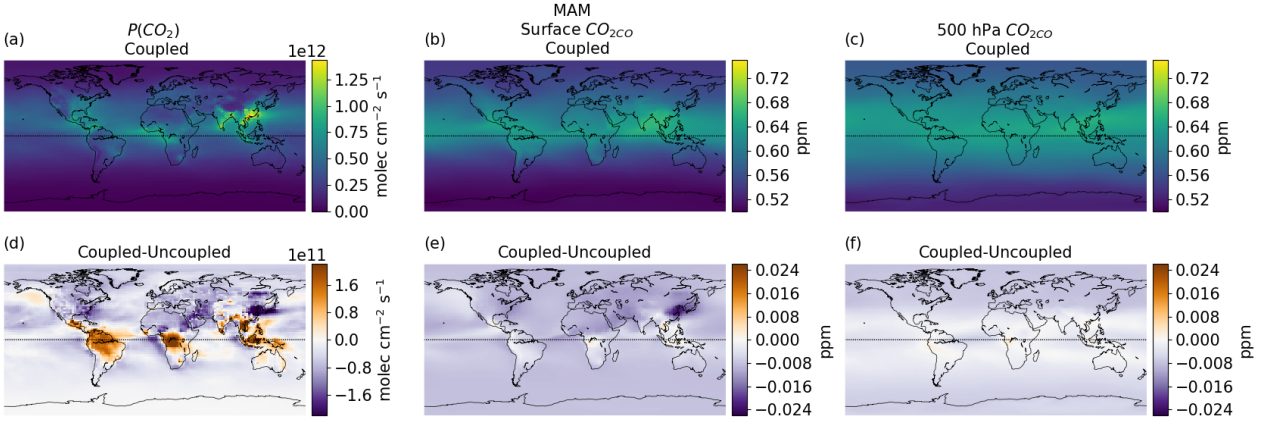


Figure S12. Average March–April–May (MAM) 2006–2017 total column CO_2 chemical production from CO (a) and corresponding mole fractions (i.e., CO_{2CO}) at the surface (b) and at 500 hPa (c) from the coupled simulation along with the difference in each field between the coupled and uncoupled simulation (d–f).

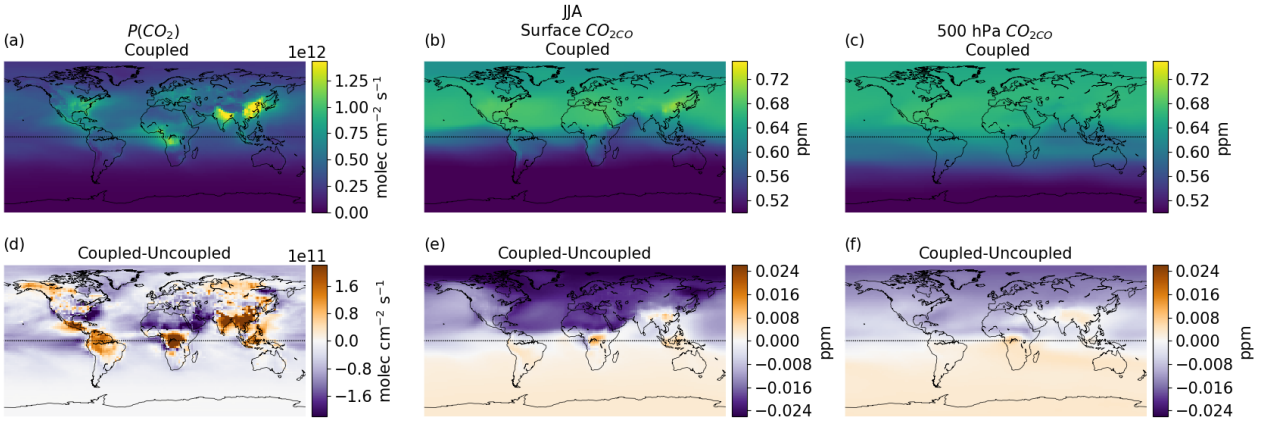


Figure S13. Average June–July–August (JJA) 2006–2017 total column CO_2 chemical production from CO (a) and corresponding mole fractions (i.e., CO_{2CO}) at the surface (b) and at 500 hPa (c) from the coupled simulation along with the difference in each field between the coupled and uncoupled simulation (d–f).

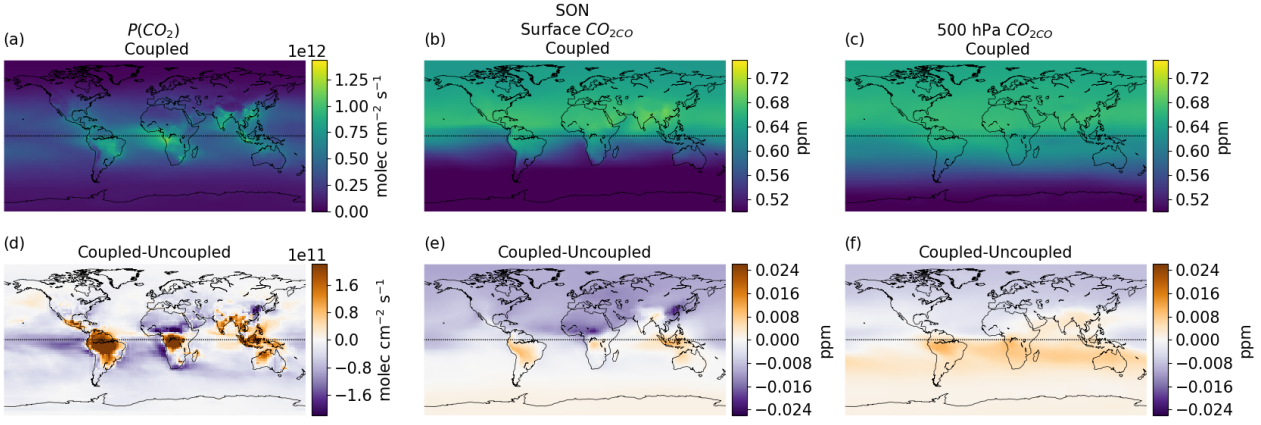


Figure S14. Average September–October–November (SON) 2006–2017 total column CO_2 chemical production from CO (a) and corresponding mole fractions (i.e., CO_{2CO}) at the surface (b) and at 500 hPa (c) from the coupled simulation along with the difference in each field between the coupled and uncoupled simulation (d–f).

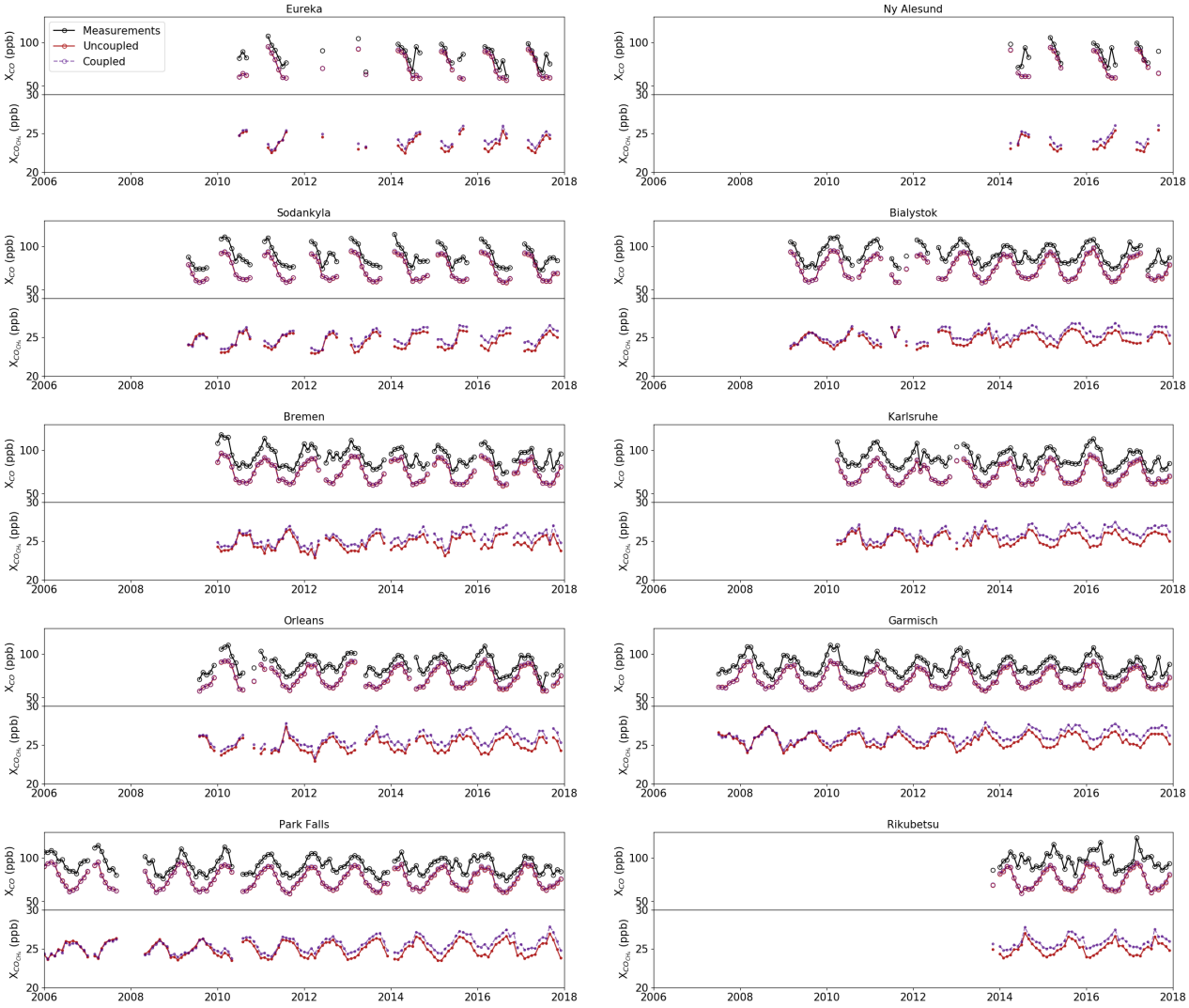


Figure S15. Modelled CO (red-uncoupled, indigo-coupled) comparison with column measurements (black) at different TCCON sites (top plots), based on monthly average values. Note, the plots show the scaled CO TCCON values (see main text for details). The bottom plots represent the mixing ratios of the CO production from CH_4 from the different simulations. Note, Eq. 14 (main text) cannot be directly used when calculating the column-averaged dry-air mole fractions of the chemical terms (i.e., CO_{2CO} and CO_{CH_4}) since the a priori (x_a) represents the profile of the total amount of each gas and has no information about the individual source contributions. The contribution of the a priori profiles is excluded for the calculation of CO_{CH_4}, which is converted to column-averaged dry-air mole fractions according to $c_s = h^T a^T x_m$.

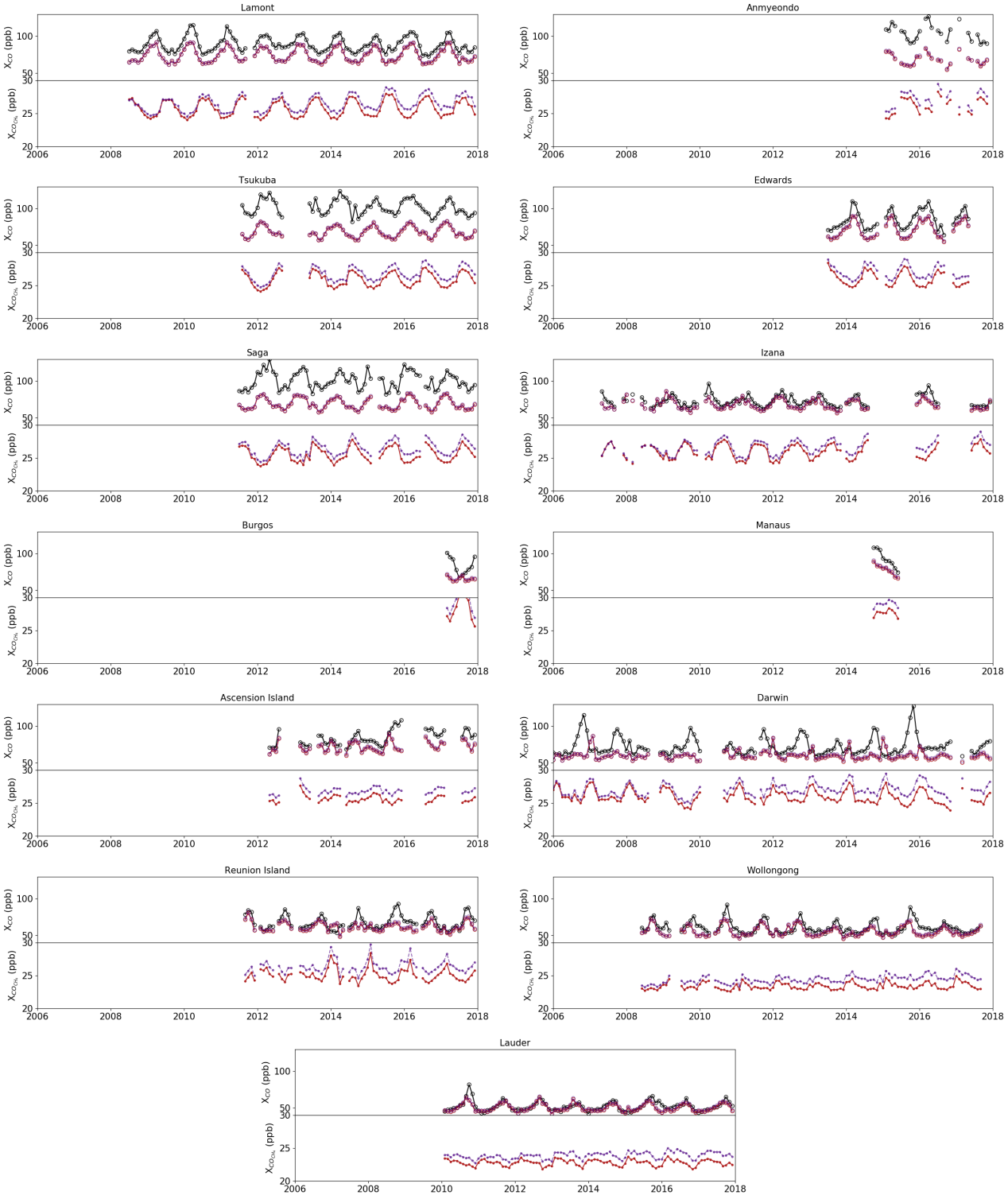


Figure S15. Continued.

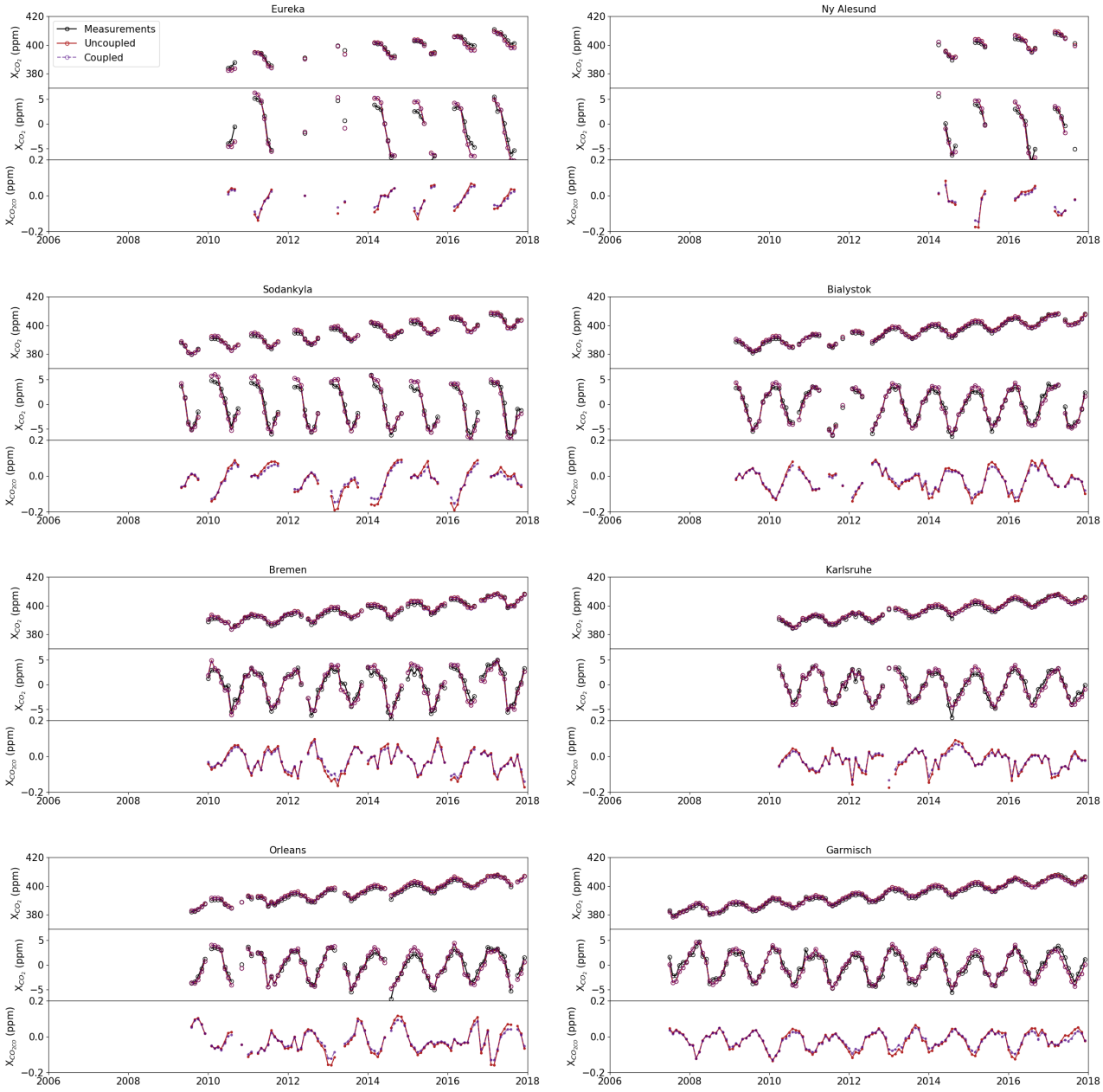


Figure S16. Modelled CO_2 (red-uncoupled, indigo-coupled) comparison with column measurements (black) at different TCCON sites (top plots), based on monthly average values. The detrended values are shown in the middle plots. The bottom plots represent the detrended mixing ratios of the CO_2 production from CO from the different simulations. Note, Eq. 14 (main text) cannot be directly used when calculating the column-averaged dry-air mole fractions of the chemical terms (i.e., CO_{2CO} and CO_{CH_4}) since the a priori (x_a) represents the profile of the total amount of each gas and has no information about the individual source contributions. The contribution of the a priori profiles is excluded for the calculation of CO_{2CO}, which is converted to column-averaged dry-air mole fractions according to $c_s = h^T a^T x_m$.

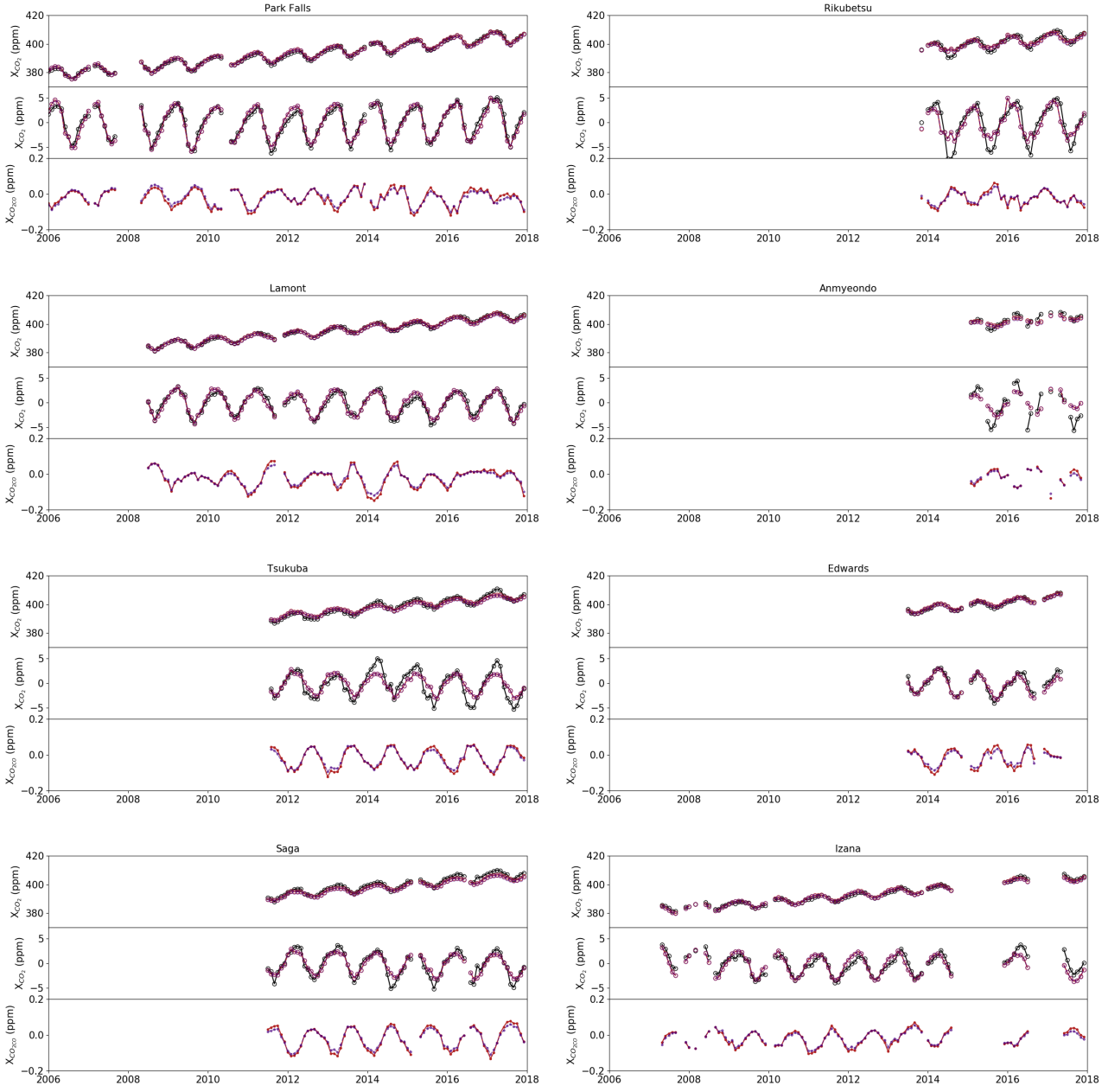


Figure S16. Continued.

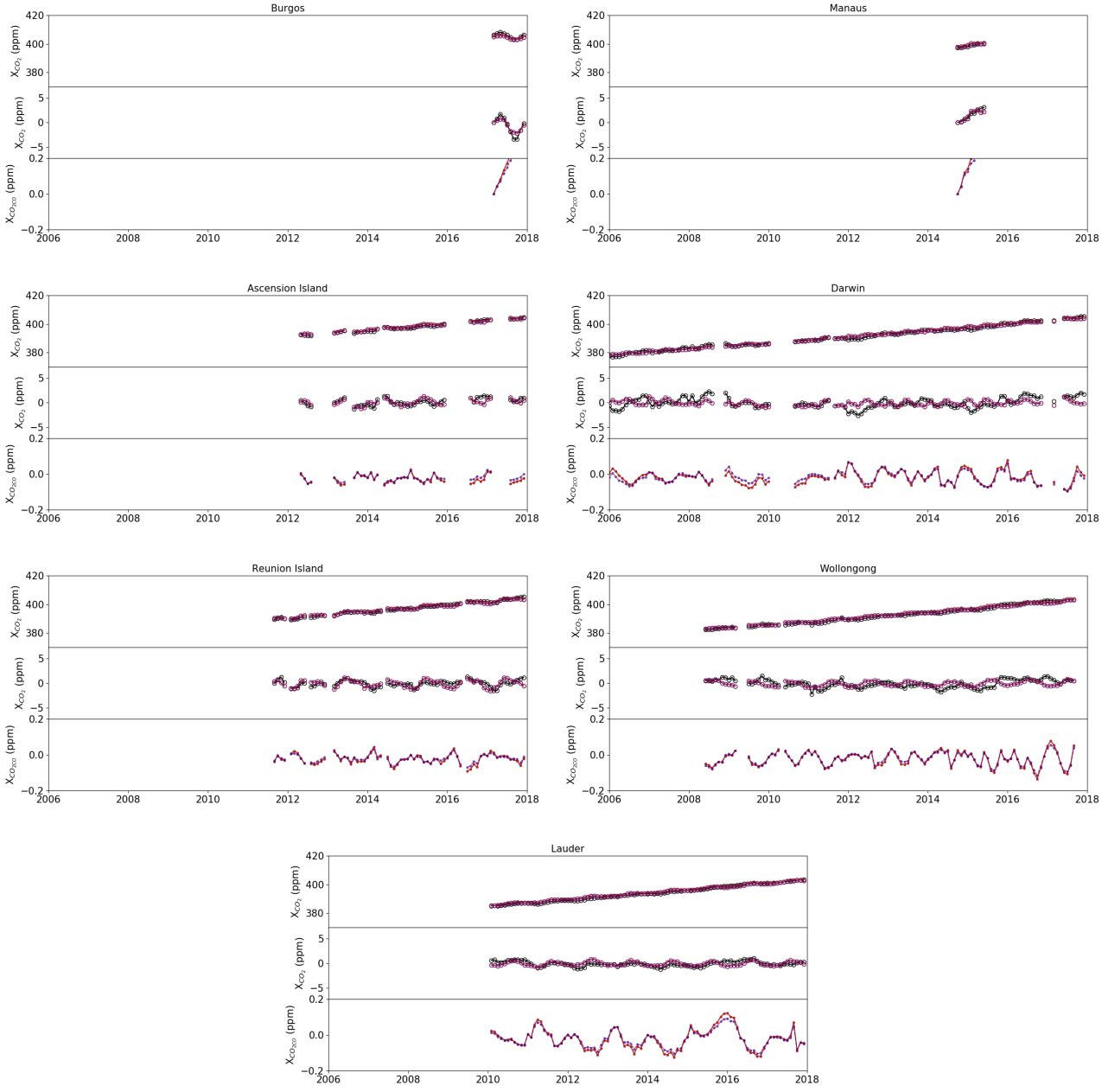


Figure S16. Continued.

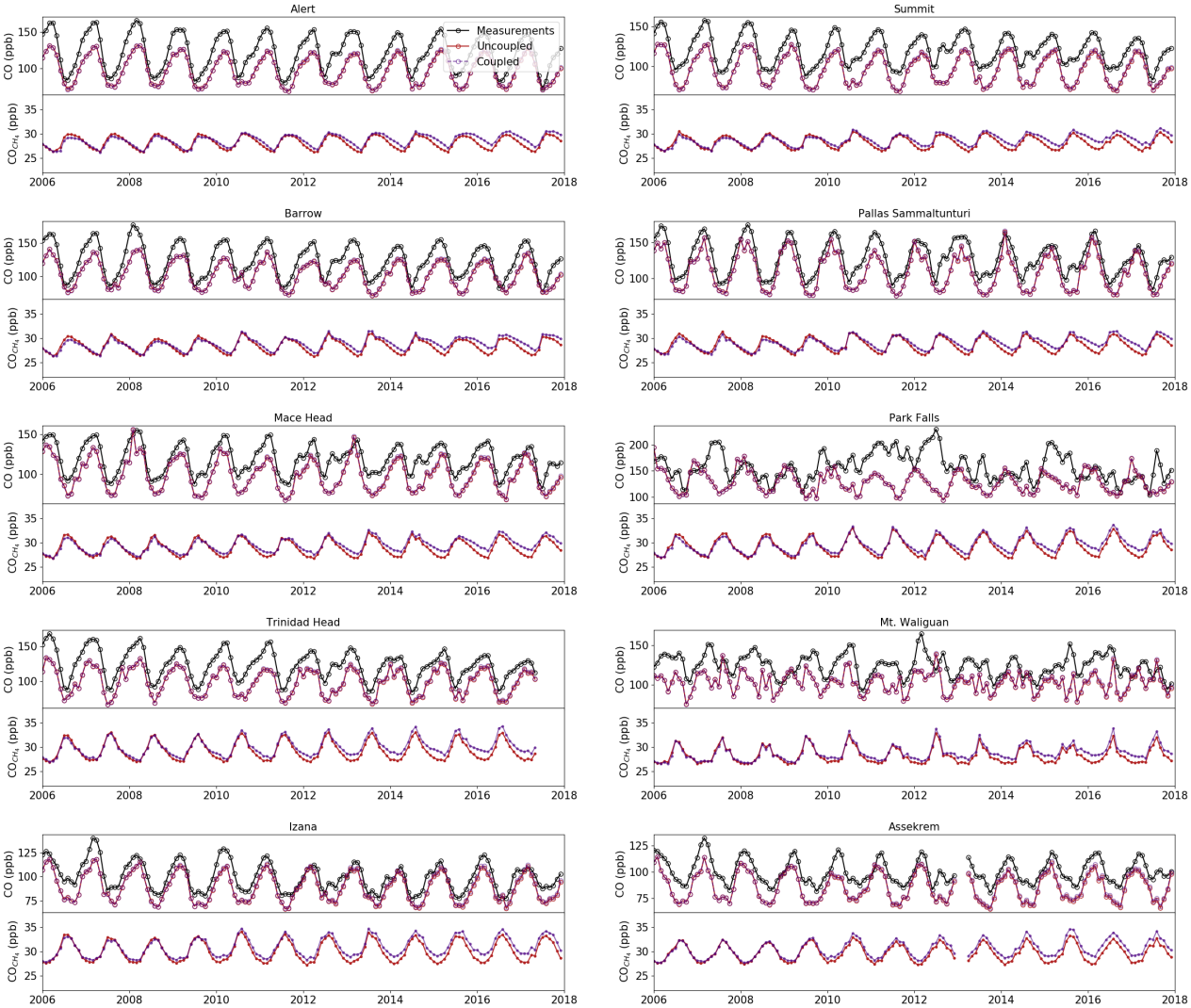


Figure S17. Modelled CO (red-uncoupled, indigo-coupled) comparison with surface measurements (black, top plots), based on monthly average values. The bottom plots represent the mixing ratios of the CO production from CH_4 from the different simulations.

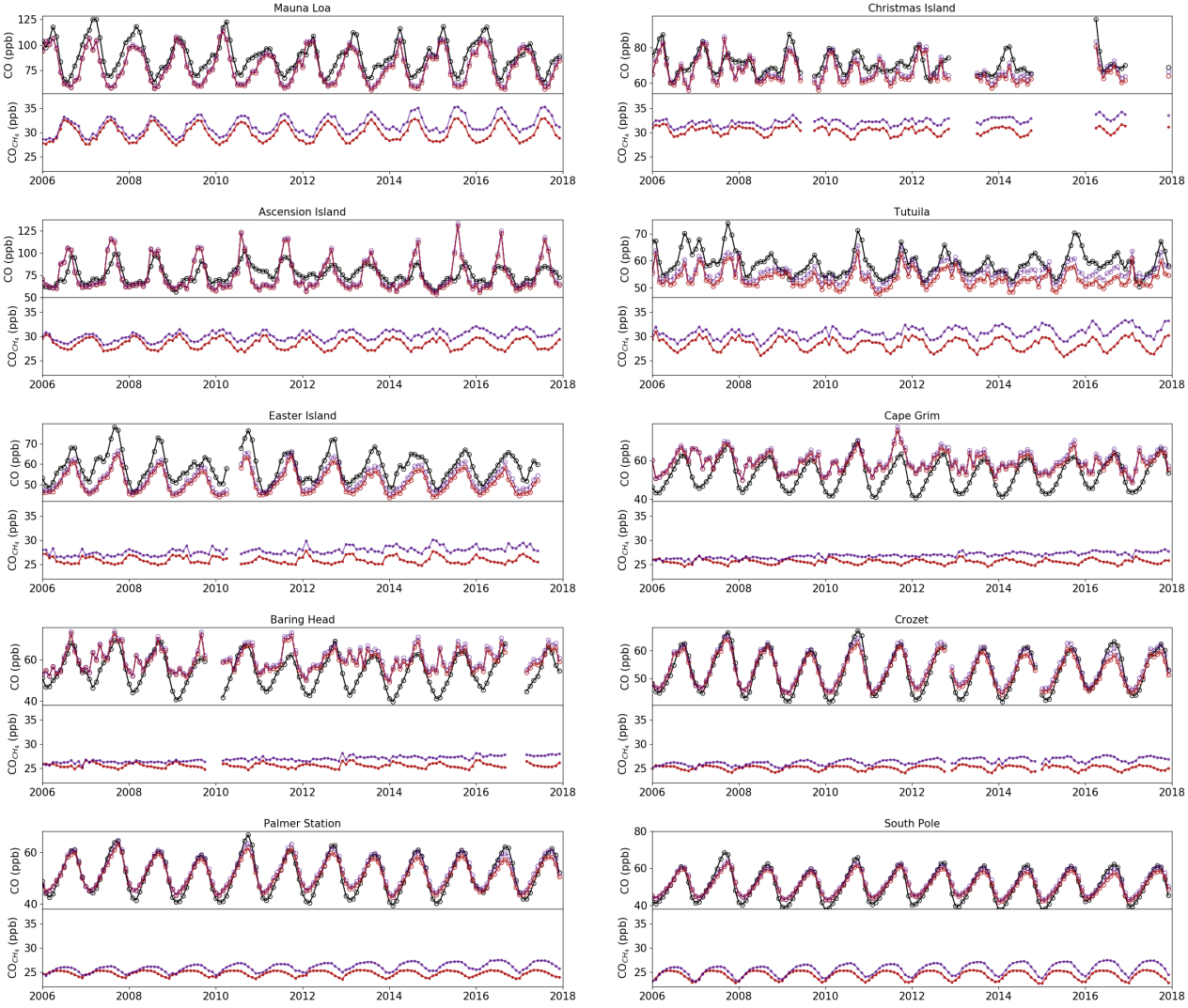


Figure S17. Continued.

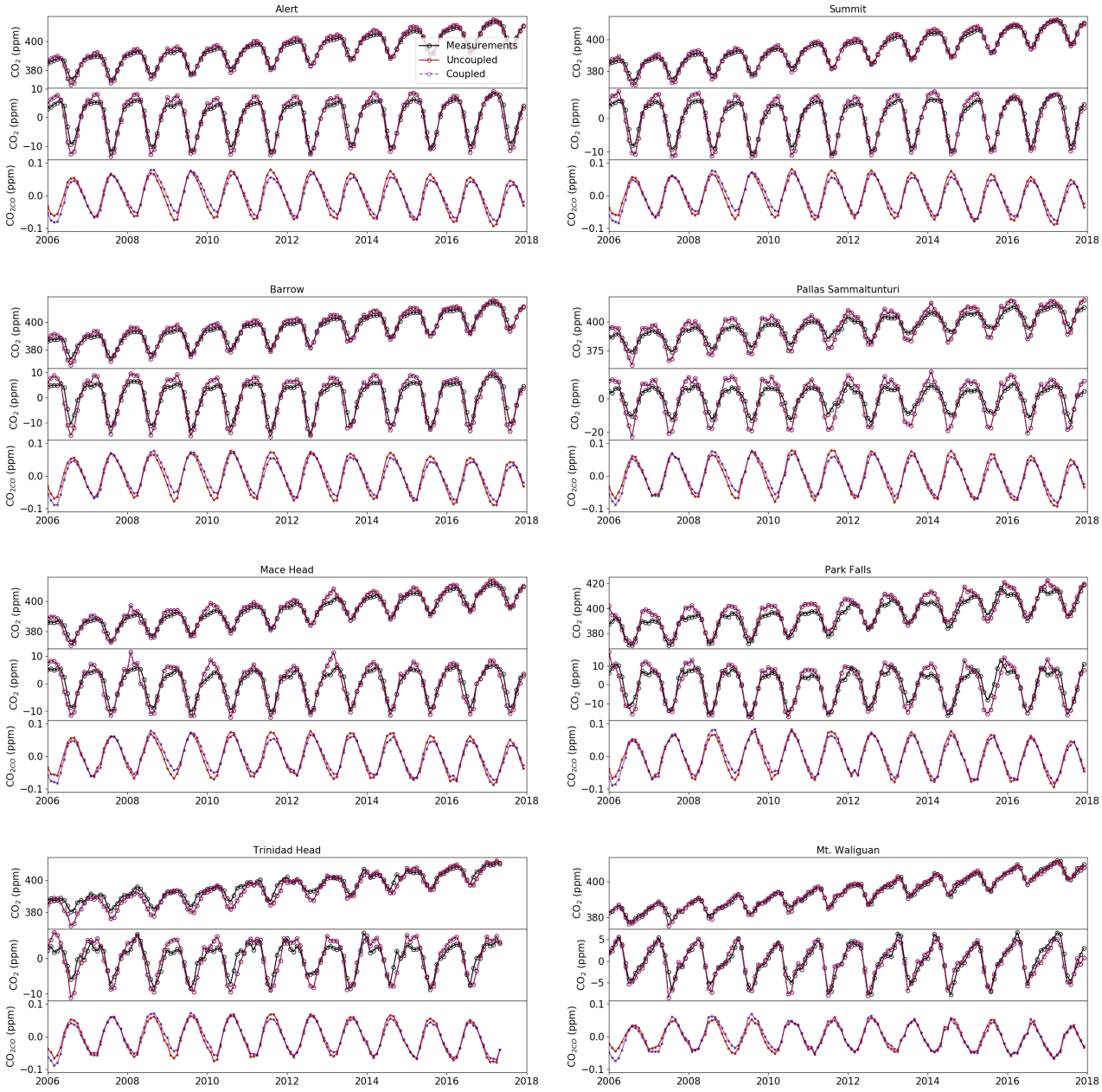


Figure S18. Modelled CO_2 (red-uncoupled, indigo-coupled) comparison with surface measurements (black, top plots), based on monthly average values. The detrended values are shown in the middle plots. The bottom plots represent the detrended mixing ratios of the CO_2 production from CO from the different simulations.

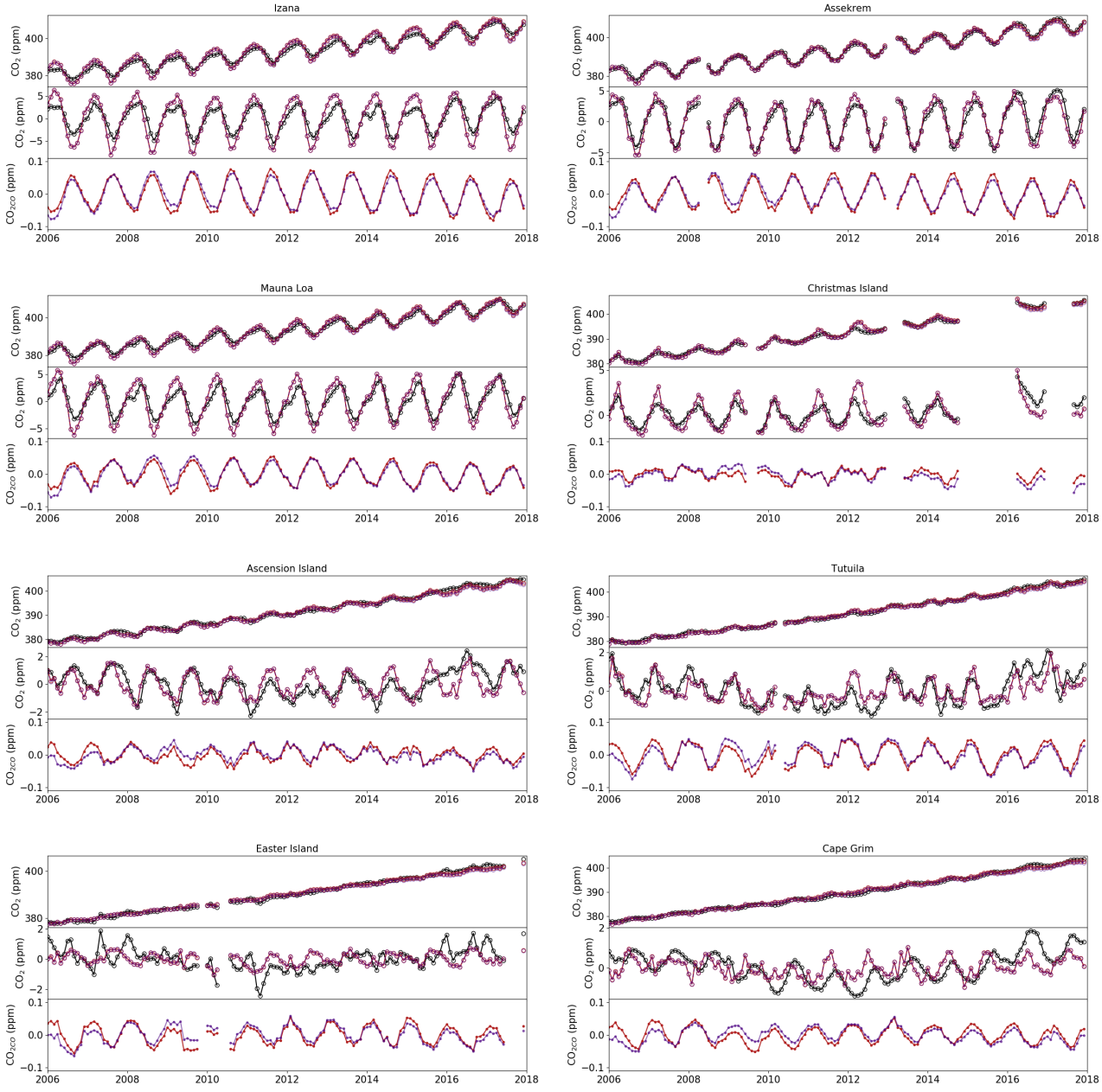


Figure S18. Continued.

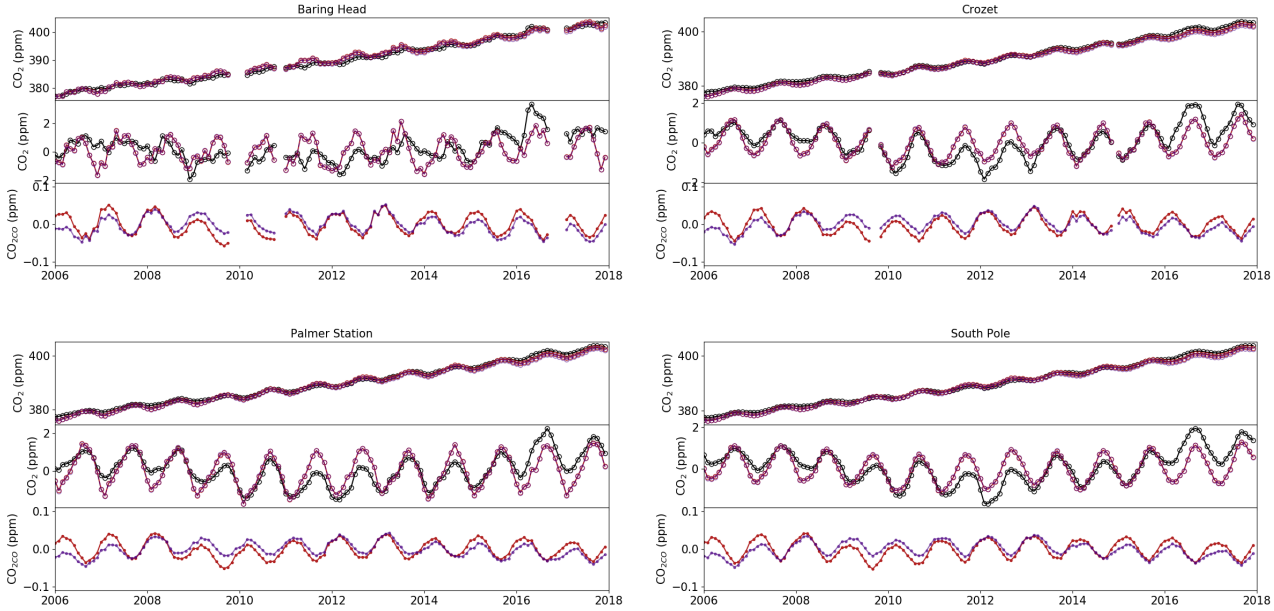


Figure S18. Continued.

S3 Comparison with aircraft measurements

Figure S20 shows the altitude versus latitude cross-sections of the CO_2 and CO chemical tracers along the ATom flight tracks. The cross-sections are constructed from linear interpolation between modelled values at the aircraft measurement locations after averaging the modelled data as described in Section 3.5 (main text).

The CO_{CH_4} values in the coupled simulation reflect the seasonal pattern in the production fields shown in Figure 7 (main text). The mole fractions are highest in the NH during borel summer (ATom 1) followed by boreal fall (ATom 3). During boreal winter (ATom 2), we see a shift of the production from the NH to the Southern Hemisphere (SH), while during boreal spring (ATom 4) we find high mole fraction values in the tropical regions. The uncoupled simulation shows a similar distribution but with overall lower values. The modelled CO_{2CO} values are more mixed throughout the atmosphere. As with CO_{CH_4}, we observe the highest CO_{2CO} values in the NH during boreal summer followed by boreal fall. In the SH, CO_{2CO} is highest during austral summer (ATom 2) but not as high as the boreal summer values in the NH. The uncoupled simulation points to higher values in the NH and lower in the SH during all seasons except during austral summer (ATom 2) when we see the opposite behavior. As shown in Figure 11 (main text), the differences in the chemical fields between simulations are also reflected in the total values of CO and CO_2.

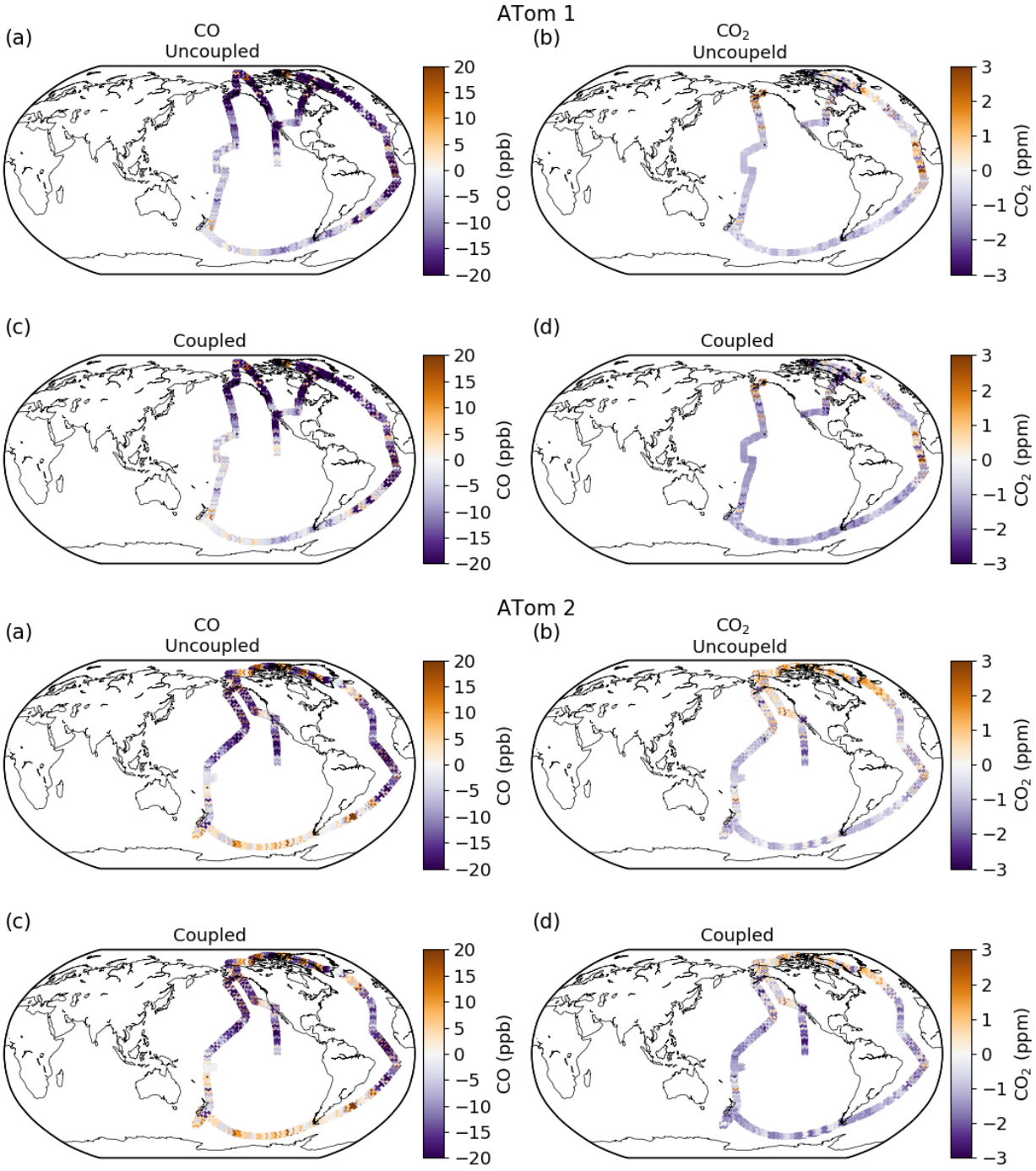


Figure S19. Model-measurement differences for CO (a, b) and CO_2 (c, d) based on simulated values from the uncoupled (a,c) and coupled (b,d) simulations during the four ATom campaigns.

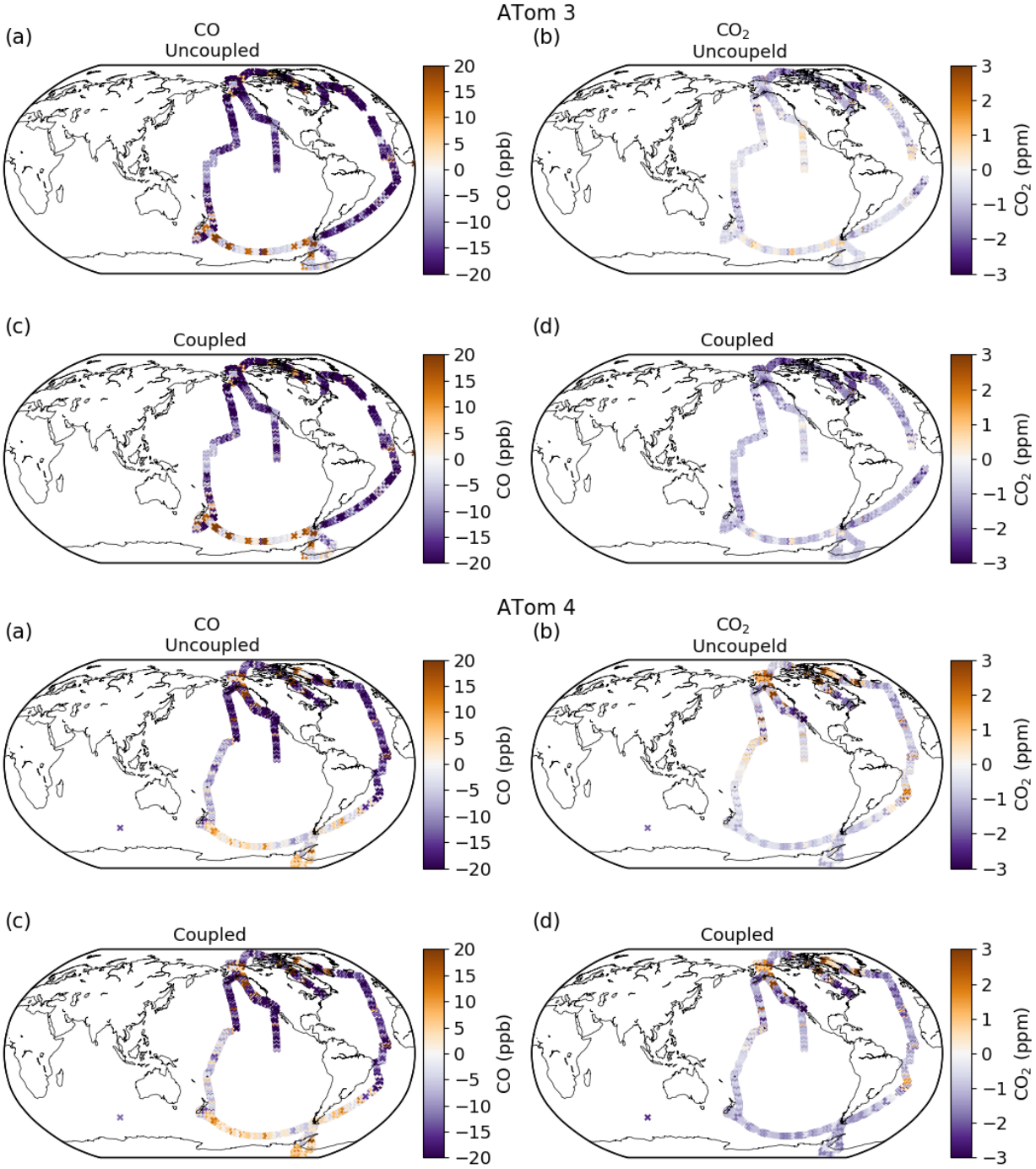


Figure S19. Continued.

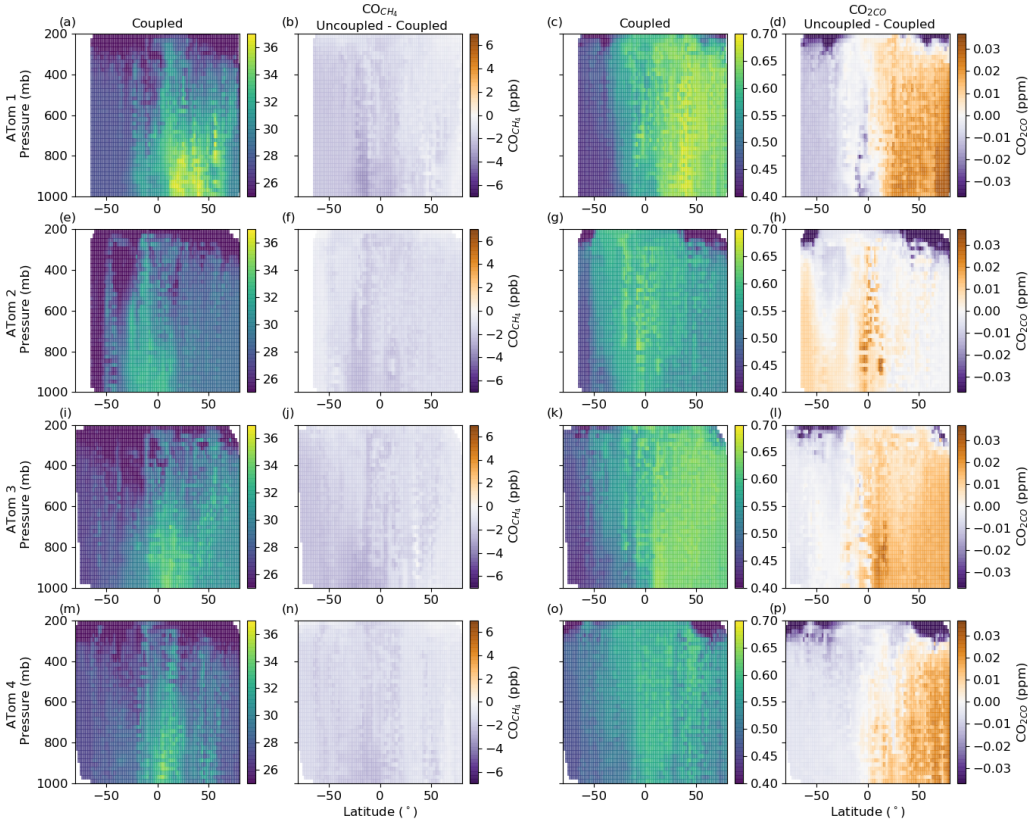


Figure S20. Altitude versus latitude cross-sections of chemically produced CO from CH_4 (CO_{CH_4}, a, b, e, f, i, j, m, n) and CO_2 (CO_{2CO}, c, d, g, h, k, l, o, p) mole fractions from the coupled simulation along with the uncoupled differences relative to the coupled simulation during the four ATom campaigns.

References

Baker, D. F., Law, R. M., Gurney, K. R., Rayner, P., Peylin, P., Denning, A. S., Bousquet, P., Bruhwiler, L., Chen, Y.-H., Ciais, P., Fung, I. Y., Heimann, M., John, J., Maki, T., Maksyutov, S., Masarie, K., Prather, M., Pak, B., Taguchi, S., and Zhu, Z.: TransCom 3 inversion intercomparison: Impact of transport model errors on the interannual variability of regional CO_2 fluxes, 1988–2003, Global Biogeochemical Cycles, 20, https://doi.org/10.1029/2004GB002439, 2006.

Bloom, A. A., Bowman, K. W., Lee, M., Turner, A. J., Schroeder, R., Worden, J. R., Weidner, R., McDonald, K. C., and Jacob, D. J.: A global wetland methane emissions and uncertainty dataset for atmospheric chemical transport models (WetCHARTs version 1.0), Geoscientific Model Development, 10, 2141–2156, https://doi.org/10.5194/gmd-10-2141-2017, 2017.

Darmenov, A. and da Silva, A.: The quick fire emissions dataset (QFED)–documentation of versions 2.1, 2.2 and 2.4, NASA Technical Report Series on Global Modeling and Data Assimilation, NASA TM-2013-104606, 32, 183, 2015.

Fung, I., John, J., Lerner, J., Matthews, E., Prather, M., Steele, L. P., and Fraser, P. J.: Three-dimensional model synthesis of the global methane cycle, Journal of Geophysical Research: Atmospheres, 96, 13 033–13 065, https://doi.org/10.1029/91JD01247, 1991.

Kuhns, H., Knipping, E. M., and Vukovich, J. M.: Development of a United States–Mexico emissions inventory for the big bend regional aerosol and visibility observational (BRAVO) study, Journal of the Air & Waste Management Association, 55, 677–692, https://doi.org/10.1080/10473289.2005.10464648, 2005.

Lee, C., Martin, R. V., van Donkelaar, A., Lee, H., Dickerson, R. R., Hains, J. C., Krotkov, N., Richter, A., Vinnikov, K., and Schwab, J. J.: SO_2 emissions and lifetimes: Estimates from inverse modeling using in situ and global, space-based (SCIAMACHY and OMI) observations, Journal of Geophysical Research: Atmospheres, 116, https://doi.org/10.1029/2010JD014758, 2011.

Li, M., Zhang, Q., Kurokawa, J.-I., Woo, J.-H., He, K., Lu, Z., Ohara, T., Song, Y., Streets, D. G., Carmichael, G. R., Cheng, Y., Hong, C., Huo, H., Jiang, X., Kang, S., Liu, F., Su, H., and Zheng, B.: MIX: a mosaic Asian anthropogenic emission inventory under the international collaboration framework of the MICS-Asia and HTAP, Atmospheric Chemistry and Physics, 17, 935–963, https://doi.org/10.5194/acp-17-935-2017, 2017.

Maasakkers, J. D., Jacob, D. J., Sulprizio, M. P., Turner, A. J., Weitz, M., Wirth, T., Hight, C., DeFigueiredo, M., Desai, M., Schmeltz, R., Hockstad, L., Bloom, A. A., Bowman, K. W., Jeong, S., and Fischer, M. L.: Gridded national inventory of US methane emissions, Environmental science & technology, 50, 13 123–13 133, https://doi.org/10.1021/acs.est.6b02878, 2016.

Maasakkers, J. D., Jacob, D. J., Sulprizio, M. P., Scarpelli, T. R., Nesser, H., Sheng, J.-X., Zhang, Y., Hersher, M., Bloom, A. A., Bowman, K. W., Worden, J. R., Janssens-Maenhout, G., and Parker, R. J.: Global distribution of methane emissions, emission trends, and OH concentrations and trends inferred from an inversion of GOSAT satellite data for 2010–2015, Atmospheric Chemistry and Physics, 19, 7859–7881, https://doi.org/10.5194/acp-19-7859-2019, 2019.

Messerschmidt, J., Parazoo, N., Wunch, D., Deutscher, N. M., Roehl, C., Warneke, T., and Wennberg, P. O.: Evaluation of seasonal atmosphere–biosphere exchange estimations with TCCON measurements, Atmospheric Chemistry and Physics, 13, 5103–5115, https://doi.org/10.5194/acp-13-5103-2013, 2013.

Oda, T. and Maksyutov, S.: A very high-resolution (1 km×1 km) global fossil fuel CO_2 emission inventory derived using a point source database and satellite observations of nighttime lights, Atmospheric Chemistry and Physics, 11, 543–556, https://doi.org/10.5194/acp-11-543-2011, 2011.

Sheng, J.-X., Jacob, D. J., Maasakkers, J. D., Sulprizio, M. P., Zavala-Araiza, D., and Hamburg, S. P.: A high-resolution (0.1° × 0.1°) inventory of methane emissions from Canadian and Mexican oil and gas systems, Atmospheric Environment, 158, 211–215, https://doi.org/10.1016/j.atmosenv.2017.02.036, 2017.

Stettler, M., Eastham, S., and Barrett, S.: Air quality and public health impacts of UK airports. Part I: Emissions, Atmospheric Environment, 45, 5415–5424, https://doi.org/10.1016/j.atmosenv.2011.07.012, 2011.

Takahashi, T., Sutherland, S. C., Wanninkhof, R., Sweeney, C., Feely, R. A., Chipman, D. W., Hales, B., Friederich, G., Chavez, F., Sabine, C., et al.: Climatological mean and decadal change in surface ocean pCO_2, and net sea–air CO_2 flux over the global oceans, Deep Sea Research Part II: Topical Studies in Oceanography, 56, 554–577, 2009.

Van Donkelaar, A., Martin, R. V., Pasch, A. N., Szykman, J. J., Zhang, L., Wang, Y. X., and Chen, D.: Improving the accuracy of daily satellite-derived ground-level fine aerosol concentration estimates for North America, Environmental science & technology, 46, 11 971–11 978, https://doi.org/doi.org/10.1021/es3025319, 2012.

Vestreng, V., Mareckova, K., Kakareka, S., Malchykhina, A., and Kukharchyk, T.: Inventory Review 2007. Stage 1 and 2 review. Emission data reported to LRTAP Convention and NEC Directive, review of gridded data and review of PM inventories in Belarus, Republic of Moldova, Russian Federation and Ukraine, 2007.

Yevich, R. and Logan, J. A.: An assessment of biofuel use and burning of agricultural waste in the developing world, Global Biogeochemical Cycles, 17, https://doi.org/10.1029/2002GB001952, 2003.